SANDIA REPORT

SAND2014-18257
Unlimited Release
Printed September 2014

A Nonlocal Peridynamic Plasticity Model for the Dynamic Flow and Fracture of Concrete

Christopher J. Lammi, Tracy J. Vogler

Prepared by
Sandia National Laboratories
Albuquerque, New Mexico 87185 and Livermore, California 94550

Sandia National Laboratories is a multi-program laboratory managed and operated by Sandia Corporation, a wholly owned subsidiary of Lockheed Martin Corporation, for the U.S. Department of Energy's National Nuclear Security Administration under contract DE-AC04-94AL85000.

Issued by Sandia National Laboratories, operated for the United States Department of Energy by Sandia Corporation.

Available to DOE and DOE contractors from
U.S. Department of Energy
Office of Scientific and Technical Information
P.O. Box 62
Oak Ridge, TN 37831

Telephone: (865) 576-8401
Facsimile: (865) 576-5728
E-Mail: reports@adonis.osti.gov
Online ordering: http://www.osti.gov/bridge

Available to the public from
U.S. Department of Commerce
National Technical Information Service
5285 Port Royal Rd
Springfield, VA 22161

Telephone: (800) 553-6847
Facsimile: (703) 605-6900
E-Mail: orders@ntis.fedworld.gov
Online ordering: http://www.ntis.gov/help/ordermethods.asp?loc=7-4-0#online

SAND2014-18257
Unlimited Release
Printed September 2014

A Nonlocal Peridynamic Plasticity Model for the Dynamic Flow and Fracture of Concrete

Christopher J. Lammi
George W. Woodruff School of Mechanical Engineering
Georgia Institute of Technology
801 Ferst Dr. NW
Atlanta, GA 30332

Tracy J. Vogler
Sandia National Laboratories
7011 East Ave.
M.S. 9042
Livermore, CA 94550

Abstract

A nonlocal, ordinary peridynamic constitutive model is formulated to numerically simulate the pressure-dependent flow and fracture of heterogeneous, quasi-brittle materials, such as concrete. Classical mechanics and traditional computational modeling methods do not accurately model the distributed fracture observed within this family of materials. The peridynamic horizon, or range of influence, provides a characteristic length to the continuum and limits localization of fracture. Scaling laws are derived to relate the parameters of peridynamic constitutive model to the parameters of the classical Drucker-Prager plasticity model. Thermodynamic analysis of associated and non-associated plastic flow is performed. An implicit integration algorithm is formulated to calculate the accumulated plastic bond extension and force state. The governing equations are linearized and the simulation of the quasi-static compression of a cylinder is compared to the classical theory. A dissipation-based peridynamic bond failure criteria is implemented to model fracture and the splitting of a concrete cylinder is numerically simulated. Finally, calculation of the impact and spallation of a concrete structure is performed to assess the suitability of the material and failure models for simulating concrete during dynamic loadings. The peridynamic model is found to

accurately simulate the inelastic deformation and fracture behavior of concrete during compression, splitting, and dynamically induced spall. The work expands the types of materials that can be modeled using peridynamics. A multi-scale methodology for simulating concrete to be used in conjunction with the plasticity model is presented. The work was funded by LDRD 158806.

Contents

Figures

This page intentionally left blank.

1 Introduction

There is significant motivation to use a nonlocal constitutive theory to model fracture in heterogeneous materials, such as concrete. The physical reasons for nonlocality in engineering materials have been summarized by Bazant [Bazant and Jirsek, 2002]. The reasons applicable to concrete include: heterogeneity of microstructure; distributed cracking is a physically observed phenomenon which cannot be simulated numerically with a local model; microcrack growth is not dependent on the local stress or strain at the crack tip, but rather the stress field within the inelastic region surrounding the crack tip; microcrack interaction, particularly the amplification or shielding of one crack by another ; and size effects on quasibrittle failure. In addition to these physical reasons, nonlocal modeling of concrete has been motivated by: The need to maintain objectivity and convergent solutions in the case of localized damage; and the need to regularize the boundary or initial-boundary value problem.

Nonlocal frameworks, both weak and strong, possess a range of influence, or characteristic length. The characteristic length, of concrete has been determined to be approximately 2.7× the maximum aggregate size [Bazant and Pijaudier Cabot, 1989]. This dimension corresponds to the strain-softening zone, or fracture process zone, ahead of a crack. A nonlocal formulation is pertinent to modeling localization and dissipation in a strain softening material since a local formulation tends to an infinitesimally small softening region and zero dissipation as the mesh size goes to zero [Belytschko et al., 1986]. This dependence is alleviated with a nonlocal formulation where nonlocal state variables serve as localization limiters.

The earliest nonlocal plasticity models were formulated by Eringen [Eringen, 1981]. His focus was not introducing localization limiters but to rather offer a continuum description of interacting dislocations and the distribution of stress ahead of a crack in ductile metals. Bazant & Lin introduced the first nonlocal model with strain softening plasticity [Bazant and Lin, 1988b]. Softening models containing an evolving nonlocal softening variable are among the simplest nonlocal models of this type, and it was shown by Planas [Planas et al., 1996] that they are equivalent to the cohesive crack model by Hillerborg [Hillerborg et al., 1976]. Other models have implemented a combination of local and nonlocal softening parameters [Strmberg and Ristinmaa, 1996]. Bazant & Lin adapted a nonlocal smeared crack model from the classical smeared crack model and stated that damage was dependent on a nonlocal average of two principal strains [Bazant and Lin, 1988a]. They found that the model reproduced Bazant's size effect law and results demonstrated objectivity to mesh orientation. Bazant & Ozbolt combined existing microplane and nonlocal damage models to create a nonlocal microplane model that accounts for fracture, damage, and size effects [Bazant et al., 1990]. The "Crush-Crack" model by diPrisco & Mazars uncoupled inelastic deformations due to crushing and cracking with nonlocal evolution equations associated with each phenomena [di Prisco and Mazars, 1996]. Their results showed that the model reproduces the behavior of concrete under multiaxial, monotonic loading. Ferrara & Prisco implemented a nonlocal damage model to study Mode I fracture in tension, 3-point bending, and wedge splitting tests [Ferrara and Prisco, 2001] based on the Crush-Crack model [di Prisco and Mazars, 1996]. Most notably, they found that fixing the characteristic length guaranteed a unique

result and by setting the characteristic length to the maximum aggregate size the fracture process zone of concrete was well-replicated. Grassl & Jirasek formulated a local plasticity model for concrete that included nonlocal damage evolution [Grassl and Jirsek, 2006].

Alternative methodologies to limit the localization of damage in strain softening materials have been formulated. Viscosity has been shown by Needleman to preserve mesh objectivity in the presence of diffuse damage [Needleman, 1988]. Additionally, the crack band model by Bazant [Bazant and Oh, 1983] and the cohesive crack model [Hillerborg et al., 1976] by Hillerborg are techniques that regularize a local continuum in the presence of damage.

The peridynamic theory of solid mechanics was first proposed by Silling to unify the mechanics of continuous and discontinuous media in a single mathematically consistent framework [Silling, 2000]. The theory states that any two material points within a finite distance can undergo thermomechanical interaction through a bond. All bond forces were considered central and independent of other neighboring bonds. This assumption leads to several restrictions on the constitutive behavior, most notably the Poisson's ratio of the material is $\frac{1}{4}$ during both elastic and inelastic deformation. To alleviate the restrictions of the original formulation, Silling et al. introduced a generalized peridynamic theory that utilized peridynamic states [Silling et al., 2007].

Two methodologies exist for modeling plasticity in peridynamics. The first utilizes an approximation of the classical deformation gradient tensor, derived by Silling et al. [Silling et al., 2007]. All other kinematic quantities used in classical constitutive modeling are calculated from the approximated deformation gradient in the traditional sense. Application of a constitutive law facilitates the calculation of stress. The second methodology is the formulation of a peridynamic plasticity model [Mitchell, 2011; Silling et al., 2007]. This model introduced a new nonlocal yield condition [Mitchell, 2011; Silling et al., 2007] and additionally was shown to adhere to the dissipation inequality of thermodynamics and was linearized under small displacement fields [Mitchell, 2011].

The comparison of peridynamics to both the cohesive finite element method (CFEM) and the extended finite element method (XFEM) in simulating dynamic crack growth through glass, PMMA, and a composite sample with a weak matrix-particle interface was performed by Agwai [Agwai et al., 2011]. It was found that all three methods produced similar crack growth speeds, however, peridynamics most accurately captured crack tip instabilities and bifurcation in glass and PMMA. It also accurately simulated the interface-debonding behavior of the composite. The effect of horizon size and discretization size on dynamic crack growth was studied by Ha [Ha and Bobaru, 2010]. It was found that crack bifurcation and the development of river patterns were independent of the either parameter, but the crack growth rates converged for horizons less than 1 mm within a simulated 40 mm glass sample. It was suggested that convergence requires the horizon at any length scale be adequately small compared to the domain size. In a subsequent publication [Ha and Bobaru, 2011], secondary cracks due to stress wave reflections at specimen boundaries were found to propagate from bifurcated crack paths, in agreement with experiment.

Most peridynamic studies have used a meshless discretization of bodies. This technique

lends well to impact problems where element distortion and other issues would limit the efficacy of finite element methods. Despite this strength, in-depth studies of impact using peridynamics are limited. Qualitative examples of the perforation of ductile plates [Macek and Silling, 2007] and penetration of concrete other brittle materials [Huang et al., 2011; Macek and Silling, 2007; Silling and Askari, 2005] have been presented. Xu [Xu et al., 2008] and Askari [Askari et al., 2011] have studied the development of internal damage in laminate composites subjected to low-velocity impact. Recently, the experimental and peridynamic analysis of the impact of a glass plate demonstrated that peridynamics replicates the fracture patterns, crack speeds, and amount of ejected impact-face material found in experiment [Hu et al., 2013]. Application of peridynamics to concrete is limited [Gerstle et al., 2007; Huang et al., 2011] and these studies do not account for the inelastic behavior of the material.

In this study, a pressure-dependent nonlocal plasticity model is formulated to study inelasticity and failure in concrete. The parameters of the model governing strength and inelastic flow are scaled, using the peridynamic horizon, to parameters in the classical Drucker-Prager model. A dissipation-based bond failure criteria is implemented to model fracture following inelastic flow with high fidelity. Numerical simulation of a single peridynamic bond along with full-scale simulations of cylinder compression, cylinder splitting, and impact induced spallation are analyzed. The model is found to replicate the behavior of concrete in each of the three loading configurations analyzed and offer distinct advantages over classical mechanics and traditional computational modeling methodologies. The work expands the types of materials that can be modeled using peridynamics. A multi-scale methodology for simulating concrete to be used in conjunction with the plasticity model is presented.

This page intentionally left blank.

2 Theoretical Framework

2.1 Peridynamic theory

Within a peridynamic body, $\mathcal{B}$, a material point, $\mathbf{x}$, interacts with all other material points, $\mathbf{x}'$, within a distance of δ, or horizon, through a peridynamic bond, $\boldsymbol{\xi}$. All of the points with a distance of δ from $\mathbf{x}$ constitute its neighborhood, $\mathcal{H}_x$. All the bonds connecting $\mathbf{x}$ to its neighborhood are called its family. In the reference configuration $\boldsymbol{\xi} = \mathbf{x}' - \mathbf{x} = \underline{\mathbf{X}}\langle\boldsymbol{\xi}\rangle$, where $\underline{\mathbf{X}}$ is the reference vector state. Any thermodynamic interaction between $\mathbf{x}$ and $\mathbf{x}'$ is permitted, but only mechanical interactions will be considered here. Application of a deformation field to $\mathcal{B}$ generates the deformed bond $\underline{\mathbf{Y}}\langle\boldsymbol{\xi}\rangle = \mathbf{y}' - \mathbf{y}$, where $\mathbf{y}'$ and $\mathbf{y}$ are the coordinates of $\mathbf{x}'$ and $\mathbf{x}$ in the current configuration and $\underline{\mathbf{Y}}$ is the deformation vector state. An illustration of a peridynamic body in the reference configuration is shown in Figure 1. Peridynamic states are bond operators and the operation on a bond is denoted with angled brackets $\langle\circ\rangle$. All vector states will be denoted with underlined, upper-case, bold Roman characters. The deformation vector state is the fundamental kinematic quantity of peridynamics, analogous to the deformation gradient tensor in the classical theory.

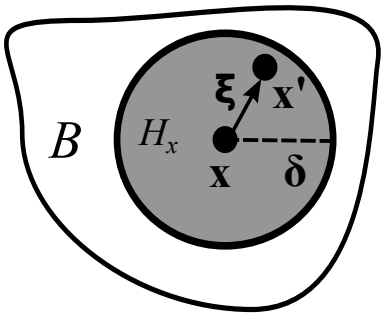

Figure 1: Illustration of a peridynamic body, $\mathcal{B}$. All material points, $\mathbf{x}'$, within the peridynamic horizon, δ, comprise the neighborhood of $\mathbf{x}$, $H_{\mathbf{x}}$, and interact via a peridynamic bond, $\boldsymbol{\xi}$.

For linear materials, the peridynamic force vector state is defined as $\underline{\mathbf{T}} = \nabla W\left(\underline{\mathbf{Y}}\right)$, where W is a scalar strain energy potential and ∇ is the Frechet derivative operator. The sum of all resulting forces at $\mathbf{x}$ is substituted into the equation of motion yielding

$$\int_{\mathcal{H}_{\mathbf{x}}} \left(\underline{\mathbf{T}}\langle\boldsymbol{\xi}\rangle - \underline{\mathbf{T}}'\langle-\boldsymbol{\xi}\rangle\right) dV_{\mathbf{x}'} + \mathbf{b} = \rho\ddot{\mathbf{u}}, \tag{1}$$

where $\mathbf{b}$ is the body force density, ρ is the density of the material, and $\ddot{\mathbf{u}}$ is the acceleration. The Frechet derivative of a scalar-valued state function, such as the elastic strain energy potential, is defined as

$$W(\underline{\mathbf{Y}} + d\underline{\mathbf{Y}}) = W(\underline{\mathbf{Y}}) + \nabla W(\underline{\mathbf{Y}}) \bullet d\underline{\mathbf{Y}} + O||d\underline{\mathbf{Y}}||. \tag{2}$$

Prior to the introduction of ordinary peridynamic materials and the focus of this work, several operators and identities in the peridynamic theory must be presented. The first is the point product of two peridynamic vector states defined as

$$\underline{\mathbf{A}} \bullet \underline{\mathbf{B}} = \int_{H_{\mathbf{x}}} \underline{\mathbf{A}}\langle\xi\rangle \cdot \underline{\mathbf{B}}\langle\xi\rangle dV_{\boldsymbol{\xi}}, \tag{3}$$

and the point product of two scalar states defined as

$$\underline{a} \bullet \underline{b} = \int_{H_{\mathbf{x}}} \underline{a}\langle\xi\rangle \underline{b}\langle\xi\rangle dV_{\boldsymbol{\xi}}. \tag{4}$$

All scalar states will be denoted by underlined, lower-case, Roman characters. The point product is a non-local, scalar quantity, dependent on all the bonds in the family of $\mathbf{x}$. Strain energy, dissipation, pressure, and dilatation are all scalar quantities requiring point product calculations. Additionally, the scalar magnitude state of a vector state is defined as $|\underline{\mathbf{A}}|\langle\xi\rangle = |\underline{\mathbf{A}}\langle\xi\rangle| = \underline{a}\langle\xi\rangle$. This relation will be used extensively in the formulation of ordinary, peridynamic materials.

2.2 Linear ordinary solids

A material is ordinary when the deformation state and force state are collinear. In this case it is convenient to simplify the reference and deformation states to scalar magnitude states, defined as $\underline{x} = |\underline{\mathbf{X}}|$ and $\underline{y} = |\underline{\mathbf{Y}}|$, respectively. The extension state is then defined as $\underline{e} = \underline{y} - \underline{x}$ and it is decomposed into isotropic and deviatoric components i.e., $\underline{e} = \underline{e}^i + \underline{e}^d$.

The strain energy potential for a linear, ordinary solid has been shown to be

$$W\left(\theta, \underline{e}^d\right) = \frac{1}{2}k\theta^2 + \frac{15\mu}{2m}\left[\underline{e}^d \bullet \left(\underline{\omega e}^d\right)\right], \tag{5}$$

where $m = (\underline{\omega x}) \bullet \underline{x}$ is a weighted volume term in the reference configuration; $\theta = \frac{3}{m}(\underline{\omega x}) \bullet \underline{e}$ is the dilatation; k and μ are the bulk and shear moduli of the material, respectively; and $\underline{\omega}$ is the influence state [Silling et al., 2007].

To avoid expressing the strain energy potential in terms of dilatation, which requires using pressure as a work conjugate, the strain energy potential is reformulated in terms of $\underline{e}^i$. Knowing that $\underline{e}^i = \frac{\theta}{3}\underline{x}$, the strain energy potential is restated as

$$W\left(\underline{e}^i, \underline{e}^d\right) = \frac{9k}{2m}\left[\underline{e}^i \bullet \left(\underline{\omega e}^i\right)\right] + \frac{15\mu}{2m}\left[\underline{e}^d \bullet \left(\underline{\omega e}^d\right)\right]. \tag{6}$$

For convenience, constants are defined to accompany the isotropic and deviatoric parts of of the strain energy, $\kappa = \frac{9k}{m}$ and $\alpha = \frac{15\mu}{m}$, yielding

$$W\left(\underline{e}^i, \underline{e}^d\right) = \frac{\kappa}{2}\left[\underline{e}^i \bullet \left(\underline{\omega e}^i\right)\right] + \frac{\alpha}{2}\left[\underline{e}^d \bullet \left(\underline{\omega e}^d\right)\right]. \tag{7}$$

Peridynamic bond forces and bond deformation are co-linear for ordinary materials, i.e.,

$$\underline{\mathbf{T}} = \underline{t}\left(\frac{\underline{\mathbf{Y}}}{|\underline{\mathbf{Y}}|}\right) = \underline{t}\underline{\mathbf{M}}, \tag{8}$$

where $\underline{\mathbf{M}}$ is the direction vector state. It then follows that the force state is defined as $\underline{t} = \nabla W$, where ∇ is the Frechet derivative operator. The force state is then

$$\underline{t} = \kappa\underline{\omega}\underline{e}^i + \alpha\underline{\omega}\underline{e}^d. \tag{9}$$

2.3 Pressure-sensitive plasticity

An ordinary plasticity model is formulated to model the pressure-dependent plastic behavior of material that is typical in brittle and quasi-brittle materials. Both the isotropic and deviatoric parts of the extension state is split into elastic and plastic parts, i.e., $\underline{e}^i = \underline{e}^{ie} + \underline{e}^{ip}$ and $\underline{e}^d = \underline{e}^{de} + \underline{e}^{dp}$, respectively. It follows that the strain energy potential of the material is restated as

$$W\left(\underline{e}^i, \underline{e}^d, \underline{e}^{ip}, \underline{e}^{dp}\right) = \frac{\kappa}{2}\left[\left(\underline{e}^i - \underline{e}^{ip}\right) \bullet \underline{\omega}\left(\underline{e}^i - \underline{e}^{ip}\right)\right] + \frac{\alpha}{2}\left[\left(\underline{e}^d - \underline{e}^{dp}\right) \bullet \underline{\omega}\left(\underline{e}^d - \underline{e}^{dp}\right)\right], \tag{10}$$

and the force state is calculated as

$$\underline{t} = \kappa\underline{\omega}\left(\underline{e}^i - \underline{e}^{ip}\right) + \alpha\underline{\omega}\left(\underline{e}^d - \underline{e}^{dp}\right). \tag{11}$$

The notation and procedure used to formulate the plasticity model follows prior work by Mitchell [Mitchell, 2011]. A space of all force scalar states $\mathcal{S}$, analogous to the Westergaard stress space, and a set within that space, $\mathcal{N}$, of allowable states is defined as

$$\mathcal{N} = \{t \in \mathcal{S} \mid F\left(\underline{t}, t_0\right) = f\left(\underline{t}\right) - t_0 \leq 0\}, \tag{12}$$

where F is the yield surface enclosing set $\mathcal{N}$, f is a function of the force scalar state, and t_0 is a material strength parameter. An illustration of the pressure-dependent yield criterion is shown in Figure 2. All force states for which $F \leq 0$ are produced by elastic deformations. For $F > 0$ the deformation is plastic. In this case the increment of plastic deformation must be calculated and the force state must return to the yield surface. For now, it is asserted that plastic flow is associated, thus, the plastic increment of the extension state is

$$\dot{\underline{e}}^p = \lambda\nabla F, \tag{13}$$

where λ is a scalar plastic multiplier and $\dot{\underline{e}}^p$ possesses both isotropic and deviatoric parts. The pressure-dependent peridynamic yield surface equation is defined as

$$F = \left(\underline{t}^d \bullet \underline{t}^d\right)^{\frac{1}{2}} - \beta p - t_0 \leq 0, \tag{14}$$

where β is an internal friction constant and p is the peridynamic pressure. The role of the second term is to include pressure dependency in the yield behavior. While stress and pressure possess consistent units, it is easily observed that the force scalar state and pressure will

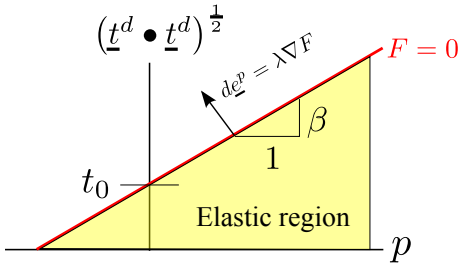

Figure 2: The pressure-dependent peridynamic yield surface, $F = 0$, separates elastic and plastic deformations within the force state space. Plastic extension is drawn outward from the surface.

not have consistent units. It will be shown later that β is not a unit-less parameter; it possesses units of length and is dependent on the size of the peridynamic horizon. Substitution of Equation 14 into Equation 13 yields

$$\dot{\underline{e}}^p = \lambda \left[\frac{\underline{t}^d}{\left(\underline{t}^d \bullet \underline{t}^d\right)^{\frac{1}{2}}} + \frac{\beta \underline{x}}{3} \right]. \tag{15}$$

Enforcing the consistency condition from classical plasticity, $\lambda \dot{F} = 0$, and utilizing the identities, $\underline{t}^d \bullet \dot{\underline{e}}^i = 0$ and $\underline{x} \bullet \dot{\underline{e}}^d = 0$, facilitates the calculation of λ to be

$$\lambda = \frac{\kappa \underline{\omega} \nabla^i F \bullet \dot{\underline{e}}^i + \alpha \underline{\omega} \nabla^d F \bullet \dot{\underline{e}}^d}{\kappa \underline{\omega} \nabla^i F \bullet \nabla^i F + \alpha \underline{\omega} \nabla^d F \bullet \nabla^d F}, \tag{16}$$

where $\nabla^i F$ and $\nabla^d F$ are the isotropic and deviatoric portions of the Frechet derivative of the yield function, respectively. By inspection, the denominator of λ is positive for any plastic increment. For elastic deformations and any deformation tangent to the yield surface it is shown that λ is zero by the consistency condition. Additionally, λ is positive for any plastic increment. Under any increment of plastic extension, the numerator of λ is also non-negative. It is observed that in the absence of isotropic forces and plastic extension increments, the flow rule presented in [Silling et al., 2007] is recovered.

2.4 Non-associated flow

For most pressure-dependent materials, the volumetric plastic strain is not accurately modeled using an associated flow rule. The peridynamic plastic flow potential is defined as

$$G = \left(\underline{t}^d \bullet \underline{t}^d\right)^{\frac{1}{2}} + \psi p, \tag{17}$$

where ψ is a dilatation constant. The increment in the plastic extension state is calculated as before to be

$$\dot{\underline{e}}^p = \lambda \left[\frac{\underline{t}^d}{\left(\underline{t}^d \bullet \underline{t}^d\right)^{\frac{1}{2}}} + \frac{\psi \underline{x}}{3} \right], \tag{18}$$

and the plastic multiplier, which is dependent on both the yield surface and flow rule becomes

$$\lambda = \frac{\kappa \underline{\omega} \nabla^i F \bullet \underline{\dot{e}}^i + \alpha \underline{\omega} \nabla^d F \bullet \underline{\dot{e}}^d}{\kappa \underline{\omega} \nabla^i G \bullet \nabla^i G + \alpha \underline{\omega} \nabla^d G \bullet \nabla^d G}. \tag{19}$$

It is clear that the properties of λ previously derived for associated flow are true for non-associated flow. The thermodynamic implications of choosing an associated or non-associated flow rule will be presented later.

2.5 Plasticity model parameter calculation

The parameters t_0, β, and ψ are related to the local, classical Drucker-Prager theory. The derivation of t_0 follows the procedure shown by Mitchell [Mitchell, 2011]. Under a purely deviatoric deformation the yield condition simplifies to be

$$\left(\underline{t}^d \bullet \underline{t}^d\right)^{\frac{1}{2}} = t_0. \tag{20}$$

In the absence of bond damage and the assumption that $\underline{\omega}\langle \boldsymbol{\xi} \rangle = 1$, the deviatoric part of the force state is $\underline{t}^d = \alpha \underline{e}^d$. It was shown by Mitchell that for purely deviatoric deformations $\left(\underline{e}^d \bullet \underline{e}^d\right)^{\frac{1}{2}} = \left(\frac{4\pi\gamma^2\delta^5}{75}\right)^{\frac{1}{2}}$, where γ is the magnitude of the shear strain [Mitchell, 2011]. Substituting these values, along with the constant α, into Equation 20 yields

$$\frac{6\mu\gamma_{max}}{m}\left(\frac{\pi\delta^5}{3}\right)^{\frac{1}{2}} = t_0. \tag{21}$$

If it is assumed that the maximum allowable shear stress is $\tau_0 = \mu\gamma_{max}$, the maximum allowable t_0 is

$$t_0 = \tau_0 \left[\frac{6}{m}\left(\frac{\pi\delta^5}{3}\right)^{\frac{1}{2}}\right]. \tag{22}$$

To determine the friction coefficient, β, a purely isotropic loading is assumed to induce yielding and the yield surface equation simplifies to

$$-\beta p_0 = t_0, \tag{23}$$

where p_0 is the failure pressure in hydrostatic tension. Substituting the value for t_0 obtained earlier yields

$$\beta = \frac{\tau_0}{-p_0}\left[\frac{6}{m}\left(\frac{\pi\delta^5}{3}\right)^{\frac{1}{2}}\right]. \tag{24}$$

It is clear that the ratio of the cohesion strength to the failure pressure is exactly $\tan(\beta_{DP})$, where β_{DP} is the friction angle in the classical Drucker Prager theory. The resulting equation for β is

$$\beta = \tan(\beta_{DP})\left[\frac{6}{m}\left(\frac{\pi\delta^5}{3}\right)^{\frac{1}{2}}\right]. \tag{25}$$

The dilatation constant, ψ, is assumed without derivation to have the same scaling to the classical Drucker-Prager dilatation angle, ψ_{DP}, as the friction angle has to the classical Drucker-Prager friction angle, i.e.,

$$\psi = \tan\left(\psi_{DP}\right)\left[\frac{6}{m}\left(\frac{\pi\delta^5}{3}\right)^{\frac{1}{2}}\right]. \tag{26}$$

2.6 Thermodynamics of associated and non-associated flow

The dissipation inequality of thermodynamics is unconditionally satisfied for associated plastic flow in classical plasticity. The associated and non-associated flow rules are analyzed to verify their adherence to the dissipation inequality following the procedure outlined by Silling & Lehoucq [Silling and Lehoucq, 2010]. Although thermodynamic admissibility is not a requirement for a constitutive law, disagreement with the First and Second Laws of Thermodynamics lacks congruency with physical understanding of the mechanical behavior of materials. Ignoring effects of temperature, the dissipation inequality for an ordinary peridynamic solid is

$$\underline{t} \bullet \underline{\dot{e}} - \dot{W} \geq 0. \tag{27}$$

Splitting the force state and increment in plastic extension state into deviatoric and isotropic parts and application of the chain rule of calculus yields

$$\left(\underline{t}^i - \frac{\partial W}{\partial \underline{e}^i}\right) \bullet \underline{\dot{e}}^i + \left(\underline{t}^e - \frac{\partial W}{\partial \underline{e}^d}\right) \bullet \underline{\dot{e}}^d - \frac{\partial W}{\partial \underline{e}^p} \bullet \underline{\dot{e}}^p \geq 0. \tag{28}$$

The first two terms reduce to zero by definition of the force state. Substitution of the constitutive model and associated flow rule yields

$$\begin{aligned} \underline{t} \bullet \underline{\dot{e}}^p &\geq 0 \\ \underline{t}^d \bullet \underline{\dot{e}}^{dp} + \underline{t} \bullet \underline{\dot{e}}^{ip} &\geq 0 \\ \lambda\left[\left(\underline{t}^d \bullet \underline{t}^d\right)^{\frac{1}{2}} - \beta p\right] &\geq 0 \\ t_0 &\geq 0. \end{aligned} \tag{29}$$

All materials possess non-negative strength, thus, it is shown that the dissipation inequality of thermodynamics is satisfied for any increment in force state. The corresponding dissipation inequality for non-associated flow reduces to

$$\frac{t_0}{p} \geq \left(\beta - \psi\right). \tag{30}$$

It is observed that the dissipation inequality is only satisfied for a finite combination of material properties and pressures. In the limit of high confining pressure, the dissipation inequality is only satisfied by associated flow.

2.7 Damage

Damage in a peridynamic material is defined as

$$\phi = 1 - \frac{\int_{\mathcal{H}_{\mathbf{x}}} d\left(\boldsymbol{\xi}\right) dV_{\boldsymbol{\xi}}}{\int_{\mathcal{H}_{\mathbf{x}}} dV_{\boldsymbol{\xi}}}, \tag{31}$$

where d is a boolean variable that equals 0 when a bond is broken and 1 otherwise. Damage models that use critical bond stretch [Silling and Askari, 2005] and critical bond strain energy density failure [Foster et al., 2011] criteria have been formulated, but neither accurately characterize the tension-compression asymmetries that exist during the failure of pressure-dependent materials. It is natural to link the damage model of the material to its constitutive model. Inelasticity in tension and shear is accommodated by the formation and growth of cracks on smaller length scales in concrete, so it is clear that inelastic dissipation in tension and shear is produced by fracture. It was shown by Foster & Silling [Foster et al., 2011] that the critical energy density for bond failure for a peridynamic material is

$$w_c = \frac{4G}{\pi\delta^4}, \tag{32}$$

where G is the critical energy release rate of the material. Under the condition that the material has yielded, the dissipation rate of a single bond, $\boldsymbol{\xi}$ is

$$\dot{w}_d = \underline{t}^i\langle\boldsymbol{\xi}\rangle\underline{\dot{e}}^{ip}\langle\boldsymbol{\xi}\rangle + \underline{t}^d\langle\boldsymbol{\xi}\rangle\underline{\dot{e}}^{dp}\langle\boldsymbol{\xi}\rangle. \tag{33}$$

Under the condition that $\int_{t_0}^{t} \dot{w}_d dt = \frac{4G}{\pi\delta^4}$, the bond is considered broken. Many cementitious materials strain soften, this effect will be modeled by the progressive failure of bonds. Fracture with strain softening of individual peridynamic bonds will not be analyzed.

This page intentionally left blank.

3 Numerical Implementation and Verification of Plasticity Model

The pressure-dependent peridynamic plasticity and damage models are implemented within the open-source peridynamic solver Peridigm [Parks et al., 2012]. Within Peridigm, bodies are discretized into material points with finite mass. As a result the integral equations governing strain energy, the equation of motion of a material point, the yield surface, and the plastic multiplier are replaced with finite sums summed over all the bonds in the family of a material point.

3.1 Numerical integration

A backward Euler numerical integration algorithm is implemented to calculate the deviatoric and isotropic parts of the plastic extension state. The approach is extension state driven and the force state is mapped back to the yield surface using a path normal to the flow potential, similar to the strain-driven approach used in classical plasticity. Subscripts of n and $n+1$ denote state values at times t and $t+\Delta t$, respectively.

Trial values of the deviatoric and isotropic force states are calculated using the constitutive laws and the deviatoric and isotropic parts of the force state at the next time step are determined to be

$$\underline{t}^d_{n+1} = \underline{t}^d_{trial} - \alpha\underline{\omega}\Delta\lambda \left[\frac{\underline{t}^d_{n+1}}{\left(\underline{t}^d_{n+1} \bullet \underline{t}^d_{n+1}\right)^{\frac{1}{2}}} \right] \tag{34}$$

and

$$\underline{t}^i_{n+1} = \underline{t}^i_{trial} - \kappa\underline{\omega}\Delta\lambda \left(\frac{\psi \underline{x}}{3} \right), \tag{35}$$

respectively, where $\Delta\lambda = \lambda\Delta t$. If the deformation is elastic, $F\left(\underline{t}_{trial}\right) \leq 0$, $\Delta\lambda = 0$, and the deviatoric and isotropic force states at the next time step will be the trial values, $\underline{t}^d_{n+1} = \underline{t}^d_{trial}$ and $\underline{t}^i_{n+1} = \underline{t}^i_{trial}$, respectively. If $F\left(\underline{t}_{trial}\right) > 0$, the deformation is inelastic and the necessary $\Delta\lambda$ to return the yield surface and the deviatoric and isotropic parts of the plastic extension state increment and force state must be calculated.

Similar to Silling [Silling et al., 2007], it is asserted that deviatoric extensions have no effect on the pressure. However, the increment in isotropic plastic extension affects the pressure and an update of the pressure must be calculated, using the increment in isotropic plastic extension, is necessary to ensure consistency. The pressure at t_{n+1} is determined to be

$$p_{n+1} = p_{trial} + k\Delta\lambda\psi. \tag{36}$$

Substitution of the yield function, Equation 14, at t_{n+1} and Equation 36 into Equation 34 yields

$$\underline{t}^d_{n+1} = \frac{\underline{t}^d_{trial}}{1 + \left[\frac{\alpha\omega\Delta\lambda}{(p_{trial} + k\Delta\lambda\psi)\beta + t_0} \right]}. \tag{37}$$

The values of $\underline{t}^d_{n+1}$ and p_{n+1} are substituted into the yield criterion at t_{n+1}, consistency is enforced, and $\Delta\lambda$ is calculated as

$$\Delta\lambda = \frac{\left(\underline{t}^d_{trial} \bullet \underline{t}^d_{trial}\right)^{\frac{1}{2}} - \beta p_{trial} - t_0}{\alpha + k\beta\psi}. \tag{38}$$

The isotropic force state, isotropic plastic extension state, and deviatoric plastic extension state immediately follow as

$$\underline{t}^i_{n+1} = \underline{t}^i_{trial} - \kappa\underline{\omega}\Delta\lambda\left(\frac{\psi\underline{x}}{3}\right), \tag{39}$$

$$\underline{e}^{ip}_{n+1} = \underline{e}^{ip}_n + \Delta\lambda\left(\frac{\psi\underline{x}}{3}\right), \tag{40}$$

and

$$\underline{e}^{dp}_{n+1} = \underline{e}^{dp}_n + \Delta\lambda\left[\frac{\underline{t}^d_{n+1}}{(\beta p_{n+1} + t_0)}\right], \tag{41}$$

respectively.

3.2 Linearization

The constitutive relations presented are linear with respect to the bond extension state, but not the displacement field. A linearized version of the kinematics and constitutive relations follow. The linearized theory will provide an exact solution for the modulus state, $\mathbb{K}$, analogous to the 4^{th} order elastic stiffness tensor, C_{ijkl}, from classical mechanics.

The displacement vector state, $\underline{\mathbf{U}}$, associated with the displacement field, $\mathbf{u}$, is defined as

$$\underline{\mathbf{U}}\left[\mathbf{x}, t\right]\langle\boldsymbol{\xi}\rangle = \mathbf{u}\left(\mathbf{q}, t\right) - \mathbf{u}\left(\mathbf{x}, t\right), \tag{42}$$

where $\boldsymbol{\xi} = \mathbf{q} - \mathbf{x}$. The displacement field is assumed to have small magnitude. The force state after the superposition of the small increment in the displacement field is

$$\underline{\mathbf{T}}\left(\underline{\mathbf{Y}}^0 + d\underline{\mathbf{U}}\right) = \underline{\mathbf{T}}\left(\underline{\mathbf{Y}}^0\right) + \underline{\mathbb{K}} \bullet d\underline{\mathbf{U}}. \tag{43}$$

The modulus state, $\underline{\mathbb{K}}$, is a double state defined as

$$\underline{\mathbb{K}} = \nabla\underline{\mathbf{T}}\left(\underline{\mathbf{Y}}^0\right). \tag{44}$$

Linearization of the pressure-dependent model follows a similar procedure as done by Silling [Silling, 2010] and later by Mitchell [Mitchell, 2011]. The kinematic variables $\underline{e}$, $\underline{e}^d$, θ, and $\underline{\mathbf{M}}$ are first linearized, followed by the pressure-dependent constitutive model.

Linearization of the extension state, $\underline{e}$, for small displacements yields

$$\begin{aligned}
\nabla\underline{e} \bullet \underline{\mathbf{U}} &= \frac{\partial}{\partial\epsilon}\left[\left(\underline{\mathbf{Y}}^0 + \epsilon\underline{\mathbf{U}}\right) \cdot \left(\underline{\mathbf{Y}}^0 + \epsilon\underline{\mathbf{U}}\right)\right]^{\frac{1}{2}}|_{\epsilon=0} \\
&= \underline{\mathbf{M}} \bullet \underline{\mathbf{U}} \\
&= \int \Delta\left(\boldsymbol{\xi} - \boldsymbol{\eta}\right)\underline{\mathbf{M}}\left(\underline{\mathbf{Y}}^0\right)\langle\boldsymbol{\xi}\rangle \cdot \underline{\mathbf{U}}\langle\boldsymbol{\xi}\rangle dV_{\boldsymbol{\xi}},
\end{aligned} \tag{45}$$

where Δ is the Dirac delta function. Linearization of the dilatation, $\theta = \frac{3}{m}\left(\underline{\omega x} \bullet \underline{e}\right)$, naturally follows as

$$\begin{aligned}\nabla\theta \bullet \underline{\mathbf{U}} &= \frac{\partial}{\partial\epsilon}\theta\left(\underline{\mathbf{Y}}^0 + \epsilon\underline{\mathbf{U}}\right)|_{\epsilon=0} \\ &= \frac{3}{m}\left(\underline{\omega x}\underline{\mathbf{M}} \bullet \underline{\mathbf{U}}\right) \\ &= \frac{3}{m}\int \underline{\omega}\left(|\boldsymbol{\xi}|\right)|\boldsymbol{\xi}|\underline{\mathbf{M}}\left(\underline{\mathbf{Y}}^0\right)\langle\boldsymbol{\xi}\rangle \cdot \underline{\mathbf{U}}\langle\boldsymbol{\xi}\rangle dV_{\boldsymbol{\xi}}.\end{aligned} \tag{46}$$

Computation of the linearized extension state and dilatation permits the simple calculation of the linearized deviatoric extension state as

$$\begin{aligned}\nabla\underline{e}^d \bullet \underline{\mathbf{U}} &= \frac{\partial}{\partial\epsilon}\underline{e}^d\left(\underline{\mathbf{Y}}^0 + \epsilon\underline{\mathbf{U}}\right)|_{\epsilon=0} \\ &= \frac{\partial}{\partial\epsilon}\left[\underline{e}\left(\underline{\mathbf{Y}}^0 + \epsilon\underline{\mathbf{U}}\right) - \frac{\theta\underline{x}}{3}\left(\underline{\mathbf{Y}}^0 + \epsilon\underline{\mathbf{U}}\right)\right]|_{\epsilon=0} \\ &= \underline{\mathbf{M}} \bullet \underline{\mathbf{U}} - \frac{1}{m}\left(\underline{x\omega x}\underline{\mathbf{M}} \bullet \underline{\mathbf{U}}\right) \\ &= \int \Delta\left(\boldsymbol{\xi} - \boldsymbol{\eta}\right)\underline{\mathbf{M}}\left(\underline{\mathbf{Y}}^0\right)\langle\boldsymbol{\xi}\rangle \cdot \underline{\mathbf{U}}\langle\boldsymbol{\xi}\rangle dV_{\boldsymbol{\xi}} \\ &\quad - \frac{1}{m}\int \underline{\omega}\left(|\boldsymbol{\xi}|\right)|\boldsymbol{\xi}|^2\underline{\mathbf{M}}\left(\underline{\mathbf{Y}}^0\right)\langle\boldsymbol{\xi}\rangle \cdot \underline{\mathbf{U}}\langle\boldsymbol{\xi}\rangle dV_{\boldsymbol{\xi}}.\end{aligned} \tag{47}$$

Finally, linearization of the direction vector state yields

$$\begin{aligned}\nabla\underline{\mathbf{M}} \bullet \underline{\mathbf{U}} &= \frac{\partial}{\partial\epsilon}\underline{\mathbf{M}}\left(\underline{\mathbf{Y}}^0 + \epsilon\underline{\mathbf{U}}\right)|_{\epsilon=0} \\ &= \left[\frac{\mathbf{I} - \underline{\mathbf{M}}\left(\underline{\mathbf{Y}}^0\right)\langle\boldsymbol{\xi}\rangle \otimes \underline{\mathbf{M}}\left(\underline{\mathbf{Y}}^0\right)\langle\boldsymbol{\xi}\rangle}{|\underline{\mathbf{Y}}^0|\langle\boldsymbol{\xi}\rangle}\right]\underline{\mathbf{U}} \\ &= \int \Delta\left(\boldsymbol{\xi} - \boldsymbol{\eta}\right)\left[\frac{\mathbf{I} - \underline{\mathbf{M}}\left(\underline{\mathbf{Y}}^0\right)\langle\boldsymbol{\xi}\rangle \otimes \underline{\mathbf{M}}\left(\underline{\mathbf{Y}}^0\right)\langle\boldsymbol{\xi}\rangle}{|\underline{\mathbf{Y}}^0|\langle\boldsymbol{\xi}\rangle}\right]\underline{\mathbf{U}}dV_{\boldsymbol{\eta}}.\end{aligned} \tag{48}$$

The linearized force vector state is

$$\nabla\underline{\mathbf{T}} \bullet \underline{\mathbf{U}} = \left(\nabla\underline{t}\underline{\mathbf{M}} + \underline{t}\nabla\underline{\mathbf{M}}\right) \bullet \underline{\mathbf{U}}. \tag{49}$$

The incremental force state equations for the pressure-dependent model are now substituted into Equation 49, i.e.,

$$\nabla\underline{t}_{n+1} \bullet \underline{\mathbf{U}} = \left(\nabla\underline{t}^i_{n+1} + \nabla\underline{t}^d_{n+1}\right) \bullet \underline{\mathbf{U}}. \tag{50}$$

Substitution of the isotropic part of the force state yields

$$\begin{aligned}\nabla\underline{t}^i_{n+1} \bullet \underline{\mathbf{U}} &= \nabla\left[\underline{t}^i_{trial} - \kappa\underline{\omega}\Delta\lambda\left(\frac{\psi\underline{x}}{3}\right)\right] \bullet \underline{\mathbf{U}} \\ &= \frac{\kappa}{3}\left(\underline{\omega x}\nabla\theta\right) \bullet \underline{\mathbf{U}} - \frac{\kappa\psi}{3}\left(\underline{\omega x}\nabla\Delta\lambda\right) \bullet \underline{\mathbf{U}}.\end{aligned} \tag{51}$$

The plastic multiplier, $\Delta\lambda$, must also be linearized and follows as

$$\begin{aligned}\nabla\Delta\lambda \bullet \underline{\mathbf{U}} &= \frac{1}{\gamma}\nabla\left[\left(\underline{t}^d_{trial} \bullet \underline{t}^d_{trial}\right)^{\frac{1}{2}} - \beta p_{trial} - t_0\right] \bullet \underline{\mathbf{U}} \\ &= \frac{1}{\gamma}\left[\frac{t^d_{trial}}{\left(\underline{t}^d_{trial} \bullet \underline{t}^d_{trial}\right)^{\frac{1}{2}}}\nabla\underline{t}^d_{trial} + \beta k \nabla\theta\right] \bullet \underline{\mathbf{U}},\end{aligned} \tag{52}$$

where $\gamma = \alpha + k\beta\psi$ and $\nabla\underline{t}^d_{trial} \bullet \underline{\mathbf{U}} = \alpha\underline{\omega}\left[\underline{\mathbf{M}}\left(\underline{\mathbf{Y}}^0\right) \bullet \underline{\mathbf{U}} - \frac{1}{3}\underline{x}\left(\nabla\theta \bullet \underline{\mathbf{U}}\right)\right]$. Assembling the terms for the isotropic part of the force state and noting that $\int \underline{t}^d_{trial}\langle\boldsymbol{\xi}\rangle\underline{x}\langle\boldsymbol{\xi}\rangle dV_{\boldsymbol{\xi}} = 0$ [Silling et al., 2007] yields

$$\begin{aligned}\nabla\underline{t}^i_{n+1} \bullet \underline{\mathbf{U}} &= \left(\frac{3k}{m} - \frac{3k^2\beta\psi}{\gamma m}\right)\left(\underline{\omega}\underline{x}\nabla\theta\right) \bullet \underline{\mathbf{U}} \\ &= \left(\frac{9k}{m^2} - \frac{9k^2\beta\psi}{\gamma m^2}\right)\int \underline{\omega}^2\left(|\boldsymbol{\xi}|\right)|\boldsymbol{\xi}|^2\underline{\mathbf{M}}\left(\underline{\mathbf{Y}}^0\right)\langle\boldsymbol{\xi}\rangle \cdot \underline{\mathbf{U}}\langle\boldsymbol{\xi}\rangle dV_{\boldsymbol{\xi}}.\end{aligned} \tag{53}$$

Substitution of the deviatoric portion of the force state yields

$$\begin{aligned}\nabla\underline{t}^d_{n+1} \bullet \underline{\mathbf{U}} &= \nabla\left[\frac{\underline{t}^d_{trial}}{1 + \frac{\alpha\underline{\omega}\Delta\lambda}{(p_{trial}+k\Delta\lambda\beta)\psi + t_0}}\right] \bullet \underline{\mathbf{U}} \\ &= \frac{\alpha\left[\phi\underline{\omega}\underline{\mathbf{M}}\left(\underline{\mathbf{Y}}^0\right) - \frac{1}{3}\phi\underline{\omega}\underline{x}\left(\nabla\theta\right)\right] \bullet \underline{\mathbf{U}}}{\phi + \alpha\underline{\omega}\Delta\lambda} \\ &+ \underline{t}^d_{trial}\left[\frac{\left(k\alpha\beta\psi\underline{\omega}\Delta\lambda\nabla\Delta\lambda - k\alpha\psi\underline{\omega}\Delta\lambda\nabla\theta - \alpha\phi\underline{\omega}\nabla\Delta\lambda\right) \bullet \underline{\mathbf{U}}}{\left(\phi + \alpha\underline{\omega}\Delta\lambda\right)^2}\right] \\ &= \alpha\int \frac{\phi\underline{\omega}\left(|\boldsymbol{\xi}|\right)\underline{\mathbf{M}}\left(\underline{\mathbf{Y}}^0\right)\langle\boldsymbol{\xi}\rangle \cdot \underline{\mathbf{U}}\langle\boldsymbol{\xi}\rangle}{\phi + \alpha\underline{\omega}\Delta\lambda} dV_{\boldsymbol{\xi}} - \frac{\alpha}{m}\int \frac{\phi\underline{\omega}^2\left(|\boldsymbol{\xi}|\right)|\boldsymbol{\xi}|^2\underline{\mathbf{M}}\left(\underline{\mathbf{Y}}^0\right)\langle\boldsymbol{\xi}\rangle \cdot \underline{\mathbf{U}}\langle\boldsymbol{\xi}\rangle}{\phi + \alpha\underline{\omega}\Delta\lambda} dV_{\boldsymbol{\xi}} \\ &+ \frac{k\alpha^2\beta\psi}{\gamma}\int \frac{||\underline{t}^d_{trial}||\Delta\lambda\underline{\omega}\left(|\boldsymbol{\xi}|\right)\underline{\mathbf{M}}\langle\boldsymbol{\xi}\rangle \cdot \underline{\mathbf{U}}\langle\boldsymbol{\xi}\rangle}{\left(\phi + \alpha\underline{\omega}\Delta\lambda\right)^2} dV_{\boldsymbol{\xi}} \\ &- \frac{\alpha^2}{\gamma}\int \frac{||\underline{t}^d_{trial}||\underline{\omega}^2\left(|\boldsymbol{\xi}|\right)\Delta\lambda\phi\underline{\mathbf{M}}\langle\boldsymbol{\xi}\rangle \cdot \underline{\mathbf{U}}\langle\boldsymbol{\xi}\rangle}{\left(\phi + \alpha\underline{\omega}\Delta\lambda\right)^2} dV_{\boldsymbol{\xi}}.\end{aligned} \tag{54}$$

The isotropic and deviatoric components are combined to yield the linearized force state,

$$\begin{aligned}\nabla\underline{t}_{n+1} \bullet \underline{\mathbf{U}} &= \left(\frac{9k}{m^2} - \frac{9k^2\beta\psi}{\gamma m^2}\right)\int \underline{\omega}^2\left(|\boldsymbol{\xi}|\right)|\boldsymbol{\xi}|^2\underline{\mathbf{M}}\left(\underline{\mathbf{Y}}^0\right)\langle\boldsymbol{\xi}\rangle \cdot \underline{\mathbf{U}}\langle\boldsymbol{\xi}\rangle dV_{\boldsymbol{\xi}} \\ &+ \alpha\phi\int \frac{\underline{\omega}\left(|\boldsymbol{\xi}|\right)\underline{\mathbf{M}}\left(\underline{\mathbf{Y}}^0\right)\langle\boldsymbol{\xi}\rangle \cdot \underline{\mathbf{U}}\langle\boldsymbol{\xi}\rangle}{\phi + \alpha\underline{\omega}\Delta\lambda} dV_{\boldsymbol{\xi}} - \frac{\alpha\phi}{m}\int \frac{\underline{\omega}^2\left(|\boldsymbol{\xi}|\right)|\boldsymbol{\xi}|^2\underline{\mathbf{M}}\left(\underline{\mathbf{Y}}^0\right)\langle\boldsymbol{\xi}\rangle \cdot \underline{\mathbf{U}}\langle\boldsymbol{\xi}\rangle}{\phi + \alpha\underline{\omega}\Delta\lambda} dV_{\boldsymbol{\xi}} \\ &+ \frac{k\alpha^2\beta\psi||\underline{t}^d_{trial}||\Delta\lambda}{\gamma}\int \frac{\underline{\omega}\left(|\boldsymbol{\xi}|\right)\underline{\mathbf{M}}\langle\boldsymbol{\xi}\rangle \cdot \underline{\mathbf{U}}\langle\boldsymbol{\xi}\rangle}{\left(\phi + \alpha\underline{\omega}\Delta\lambda\right)^2} dV_{\boldsymbol{\xi}} \\ &- \frac{\alpha^2||\underline{t}^d_{trial}||\Delta\lambda\phi}{\gamma}\int \frac{\underline{\omega}^2\left(|\boldsymbol{\xi}|\right)\underline{\mathbf{M}}\langle\boldsymbol{\xi}\rangle \cdot \underline{\mathbf{U}}\langle\boldsymbol{\xi}\rangle}{\left(\phi + \alpha\underline{\omega}\Delta\lambda\right)^2} dV_{\boldsymbol{\xi}}.\end{aligned} \tag{55}$$

4 Results

4.1 Numerical simulation of a 2-point, 2-bond system

Numerical simulation of a 2-point, 2-bond peridynamic system is performed to verify that the model correctly integrates the plastic extension state, preserves consistency, and produces non-negative dissipation rates during plastic deformation. The configurations for deviatoric and isotropic deformations are shown in Figure 3. One material point is fixed; in both simulations it is the lower material point labeled S. In the deviatoric and isotropic tests, the position of the second point is translated in the x and y directions, respectively. The material point starts at x_0 or y_0 and is sequentially translated to positions 1, 2, and 3. Material properties of high-performance concrete are assigned to the bond. The elastic modulus is 53 GPa and the Poisson's ratio is 0.17 [Sorelli et al., 2008]. The cohesion strength and friction angle are chosen such that the yield strength in tension and compression are 10 MPa and 200 MPa, respectively. Associated plastic flow is assumed. In both unit tests, the initial spacing between the material points is 3 mm, corresponding to the estimated characteristic length of a high-performance concrete continuum with a maximum aggregate size of 1 mm. The force densities at which the systems will yield, for deviatoric and isotropic deformations, are analytically calculated as 1.09×10^{14} N/m^3 and 1.40×10^{10} N/m^3, respectively.

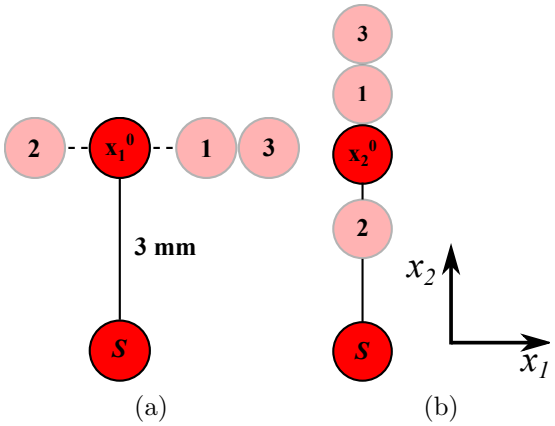

Figure 3: Unit test configuration for a 2-point, 2-bond peridynamic system for (a) deviatoric, and (b) isotropic, deformations. Stationary points in each simulation are labeled S. Points x_1^0 and x_2^0 are progressively translated in x_1 and x_2, respectively, to positions 1, 2, and 3.

The results of the unit tests for deviatoric and isotropic deformations are found in Figure 4(a) and Figure 4(b), respectively. It is found that calculated force densities and bond extensions at yield agree with the analytical solutions. The deviatoric test exhibits hysteresis and plastic consistency. The isotropic test exhibits yielding and plastic consistency in isotropic tension and linear-elastic behavior in isotropic compression. Both tests clearly demonstrate non-negative dissipation rates during plastic deformation.

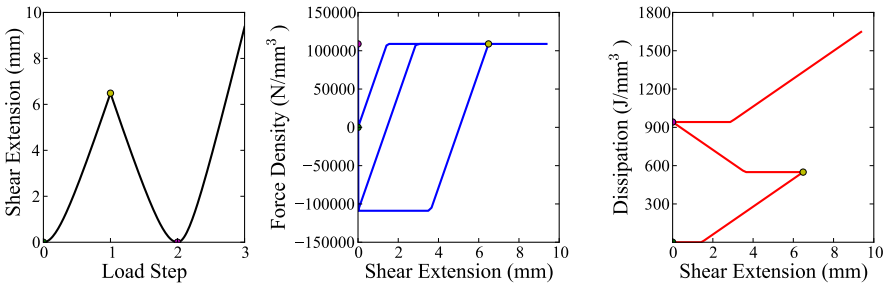

(a) Deviatoric deformation

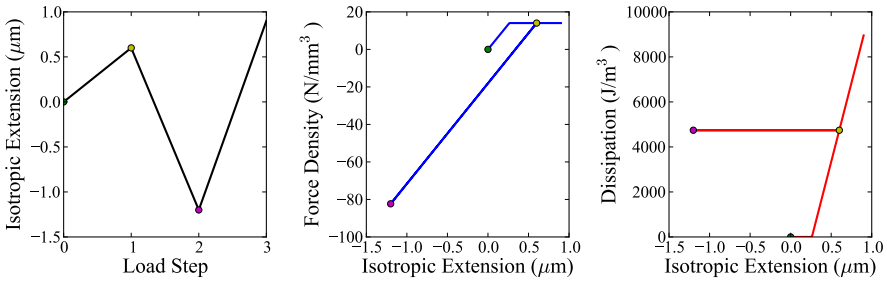

(b) Isotropic deformation

Figure 4: Unit test results for (a) deviatoric, and (b) isotropic, deformation of a 2-point, 2-bond peridynamic system. Numerical calculations agree with analytical solution for the force densities and extensions at yield. The integration algorithm accurately predicts plastic consistency and produces non-negative dissipation rates.

4.2 Quasi-static cylinder compression

The compression of a cylinder is simulated to verify that the scaling laws derived to relate t_0, β, and ψ to the parameters of the classical Drucker-Prager plasticity model are correct. The target compressive strength for all cylinder compression simulations is 200 MPa; $\tan(\beta_{DP})$ is assigned values of 0, 0.25, 0.50, 1.00, and 1.50 and the necessary t_0 to achieve a compressive strength of 200 MPa is then calculated. The model configuration is shown in Figure 5. A linearly varying displacement field of $u_3 = -0.004x_3$ is applied to all material points in the boundary volume regions, shown in blue. The reaction forces are summed over the boundary regions to determine the force necessary to compress the cylinder. Engineering stress and strain are calculated in the traditional sense. The effects of horizon size and grid refinement are analyzed.

Results for simulations performed with a nominal grid spacing, dx, of 5 mm are shown in Figure 6. The horizon size is refined from 15 mm to 7.5 mm. As the horizon is refined, the elastic modulus is found to tend towards the input value of 53 GPa, while the compressive yield strength is found to tend away from the target value of 200 MPa. Simulations with $\tan(\beta_{DP}) = 1.50$ possess poorer convergence than those with smaller $\tan(\beta_{DP})$ values.

The results of simulations performed with the smallest horizon of 7.5 mm with varying grid

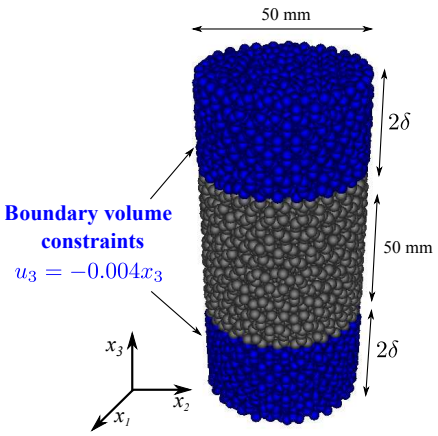

Figure 5: Cylinder compression configuration used for constitutive model comparison to the classical theory. Constant strain conditions are applied to the boundary volume regions at the top and bottom of the cylinder, shown in blue.

spacing is shown in Figure 7. As the grid spacing is decreased from 5 mm to 2.5 mm, the elastic modulus and compressive yield strength are observed to converge towards their input and target values, respectively. Even at the smallest horizon size and grid spacing analyzed, the elastic modulus differs by 10% from the input value. It is proposed that the elastic modulus would continue to converge to the input value with decreasing horizon, such that the horizon is significantly smaller than the cylinder diameter. Calculations on the surface of the cylinder are performed over, at most, half the number of points as the interior of the body, thus, point product calculations are more sensitive to heterogeneity in the volume discretization of the body. As the horizon size is decreased the influence of calculations performed over points on the surface also decreases. Additionally, it has been reported that the shear stiffness along the boundary of a body requires a correction factor [Oterkus et al., 2012].

4.3 Cylinder splitting

The splitting of a concrete cylinder is simulated to verify the engineering tensile strength calculated by the new constitutive model. The internal friction constant is the same for all simulations, $\tan(\beta_{DP}) = 1.5$. $\tan(\psi_{DP})$ is varied from zero to 1.5, corresponding to non-associative flow with no volumetric component and associated flow, respectively. The cylinder splitting model configuration is shown in Figure 8. An explicit time integration algorithm is used to solve for the plastic extension and force states at each successive time step. The smaller stable time step, inherent to explicit calculations, is better suited for maintaining stability in simulations with bond failure since it assures that fewer bonds will fail during each step. The platen at the bottom of the cylinder undergoes zero displacement in x_2 and the platen at the top is displaced in $-x_2$ at a rate of 50 mm/s. A low strain rate was chosen to remove the effects of inertia and large stress wave reflections that may

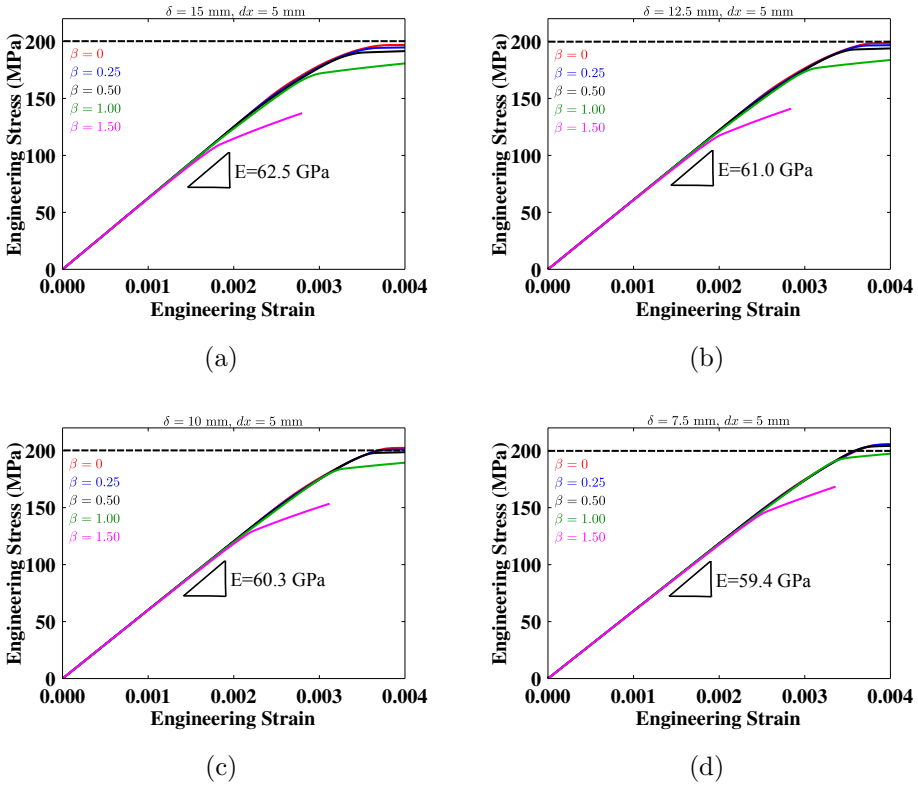

Figure 6: Stress-strain results for cylinder compression simulations with 5 mm grid spacing and horizon sizes of (a) 15 mm; (b) 12.5 mm; (c) 10 mm; and (d) 7.5 mm. The elastic modulus is found to tend towards the input value of 53 GPa, while the compressive strength tends away from the target value of 200 MPa.

influence the fracture behavior.

Representative splitting behavior is shown in Figure 9. In this particular simulation the material possessed a fracture energy of 100 J/m^2 and a dilatation constant of zero. Figure 9(a), Figure 9(b), and Figure 9(c) show the x_1 component in the displacement field when the top platen has displaced 0.02 mm, 0.04 mm, and 0.06 mm, respectively, in x_2. A displacement gradient in the x_1 direction produces tensile stresses, bond damage, and failure through the development of a critical vertical crack in the x_2 direction. The damage fields that these three stages of platen displacement are shown in Figure 9(d), Figure 9(e), and Figure 9(f), respectively. At a platen displacement of 0.04 mm, damage is found to localize at the edges of the contact region between the cylinder and platens and along a vertical path through the center of the cylinder. A critical crack, indicated by contiguous damage values of 0.5, is formed after 0.06 mm platen displacement and is then followed by failure.

The dynamic load applied to the top platen is tracked throughout the simulations. The dynamic load at failure, P_{max}, is computed and substituted into the equation $\sigma_{sp} = \frac{2P_{max}}{\pi dL}$, provided by ASTM C496 to calculate the splitting strength, σsp, where d and L are the diameter and length of the cylinder, respectively [ASTM, 2009]. The splitting stress as a

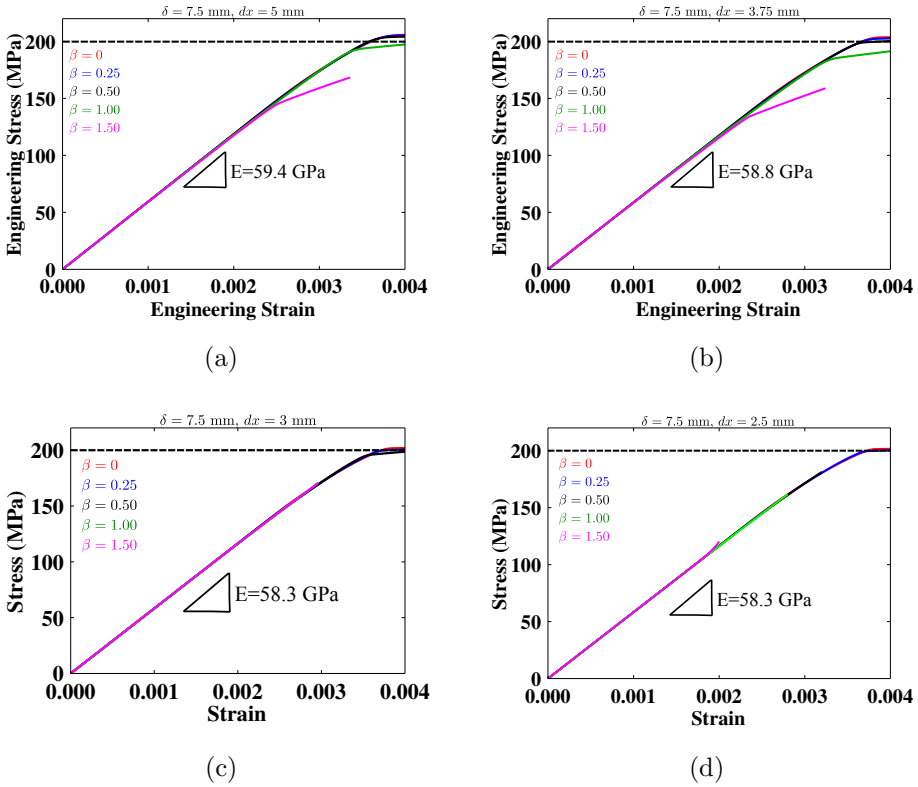

Figure 7: Stress-strain results for cylinder compression simulations with 7.5 mm horizon and grid spacing of (a) 5 mm, (b) 3.75 mm, (c) 3 mm, and (d) 2.5 mm show that the elastic modulus and yield strength converge to their input and target values with grid refinement, respectively.

function of platen displacement for cylinders with a fracture energy of 100 J/m^2 are shown in Figure 10. The splitting stress at failure is found to be higher than the target splitting stress and increases with increasing ψ. As ψ increases, the positive volumetric flow upon yielding increases. Under confinement of the platens the pressure will, thus, also increase. This increase in pressure will result in a higher splitting strength.

The splitting strength for four values of fracture energy, 10 J/m^2, 100 J/m^2, 1 kJ/m^2, and 10 kJ/m^2, plotted as a function of ψ, is shown in Figure 11. In addition to increases in ψ resulting in an effective increase in the splitting strength, increases in fracture energy are also observed to have a similar effect. Splitting strength is observed to agree with the target strength for brittle and quasi-brittle fracture energies of 10 J/m^2 to 100 J/m^2. As the fracture energy and dilatation constant are increased greater amounts of volumetric expansion occurs, increasing the pressure, and thus increasing the effective splitting strength.

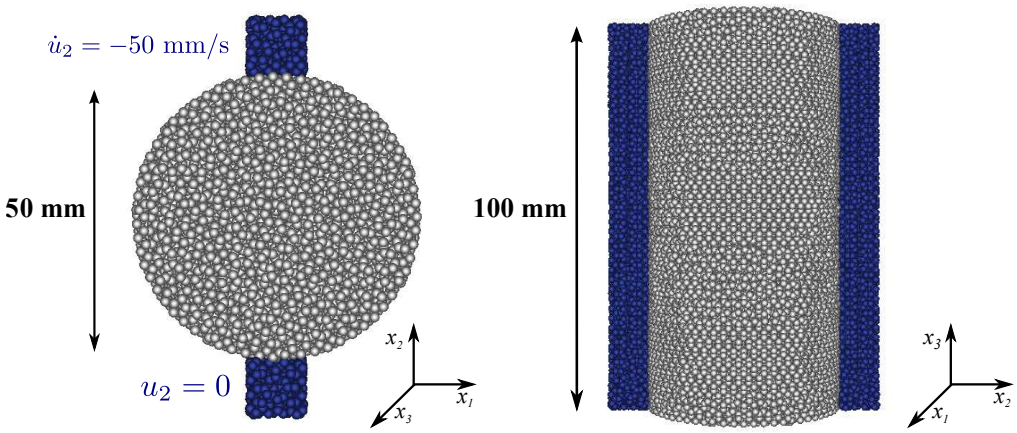

Figure 8: Engineering-scale cylinder splitting test configuration used to calculate the effective splitting strength of a concrete cylinder.

4.4 Impact and Spall

The final simulation configuration used to verify the material and damage models is the low velocity impact and spall of a concrete structure. The model configuration is shown in Figure 12. A concrete structure is idealized as a cylinder enveloped by a boundary volume region that restricts displacement in x_1 and x_2. The resulting deformation is plane strain in x_3. To induce a compressive wave, a region of thickness $2\delta_{max}$ is given an initial velocity, v_0, where δ_{max} is the maximum horizon size analyzed among all simulation models. Models with imparted initial velocities of 10 m/s, 25 m/s, and 50 m/s are analyzed. The use of a constant $2\delta_{max}$ ensures equal imparted kinetic energies, near-steady state wave propagation, and equal pulse width for all model configurations. The cylinder is modeled as a pressure-dependent solid with a compressive strength of 200 MPa, $tan\left(\beta_{DP}\right) = 1.5$, $tan\left(\psi_{DP}\right) = 0.4$, density of 2.53 g/cm^3, and $G_0 = 100$ J/m^2.

Visualization of representative damage fields and spallation after impact are shown in Figure 13. Figure 13(a), Figure 13(b), and Figure 13(c) show damage fields with v_0=10 m/s. During these simulations a crack, signified by planar damage fields with values equal to 0.5, is observed on the rear face. No front face scabbing occurs during these simulations. Figure 13(d), Figure 13(e), and Figure 13(f) show damage fields with v_0=50 m/s. Rear face spallation is observed. Additionally, fragmentation of material is more severe than in simulations with v_0=10 m/s; damage values in the spalled region range from 0.8-1. Front face scabbing is observed. The effect of horizon size and grid spacing is analyzed. Figure 13(a) and Figure 13(d) show damage fields produced with δ=15 mm and dx=5 mm; Figure 13(b) and Figure 13(e) show damage fields produced with δ=7.5 mm and dx=5 mm; and Figure 13(c) and Figure 13(f) show damage fields produced with δ=7.5 mm and dx=2.5 mm. The rear face spall depth for all model configurations is plotted as a function of imposed velocity in Figure 14(a). Spall depth does not exhibit strong dependence on the

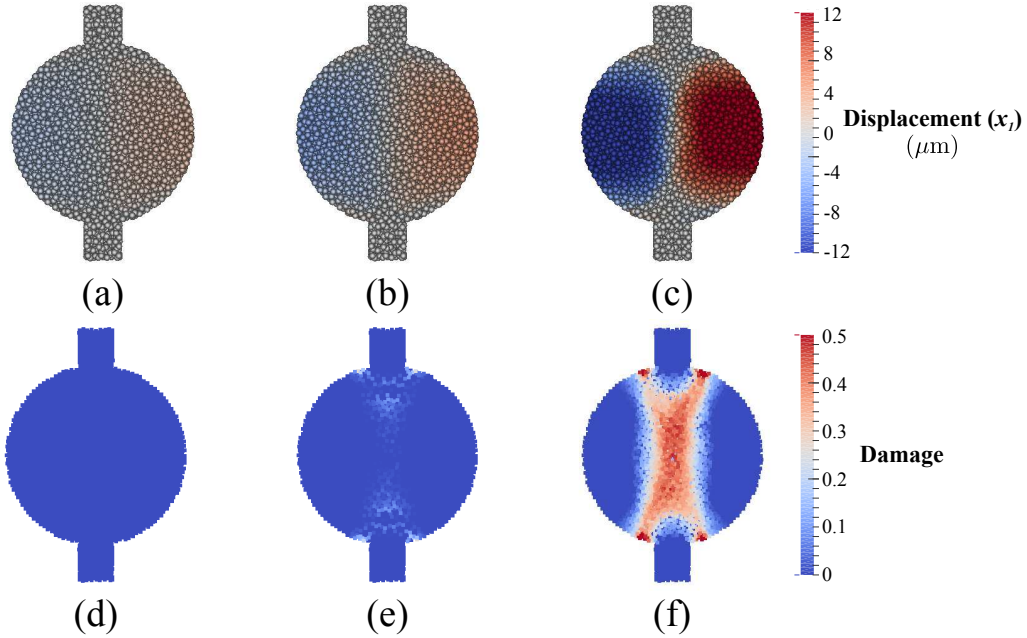

Figure 9: Representative x_1-displacement fields when the displacement of the top platen is (a) 0.02 mm, (b) 0.04 mm, and (c) 0.06 mm illustrate the displacement gradient that produces tensile σ_{11}. The resulting damage fields when the displacement of the top platen is (d) 0.02 mm, (e) 0.04 mm, and (f) 0.06 mm illustrate the initiation and propagation of a critical crack in the x_2 direction.

grid spacing, but does show dependence on the horizon size and to a lesser degree the imposed velocity. Velocity calculations on the rear surface are taken during dynamic testing. These calculations in combination with the balance on linear momentum on the free surface facilitate determination of the spall strength, $\sigma_{spall} = \frac{1}{2}\rho C_L \Delta v_{free}$, where ρ is the material density, C_L is the longitudinal wave speed in the material, and Δv_{free} is the difference between the first two peaks in the velocity profile on free surface.

The spall strength for all imposed velocities and model configurations is shown in Figure 14(b). Spall strength is observed to be independent of the strength of the imposed impact and the model configuration. Dynamic testing of ordinary, high-performance, and ultra-high performance concretes to range from 15-50 MPa [Millon et al., 2009]. The spall strengths determined from simulation are in agreement with experiment.

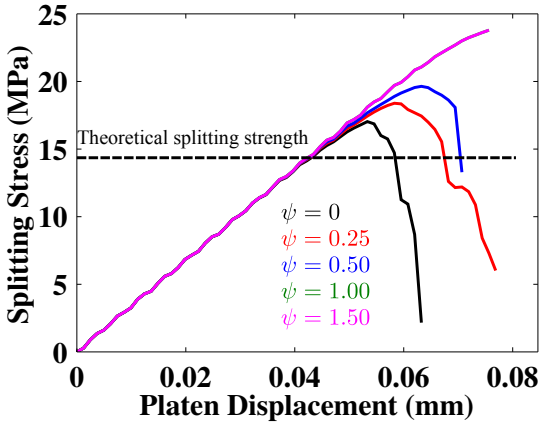

Figure 10: Splitting stress as a function of platen displacement for cylinders with a fracture energy of 100 J/m^2 plotted against the target splitting strength. Volumetric plastic extension is found to increase the strength by providing additional confinement pressure.

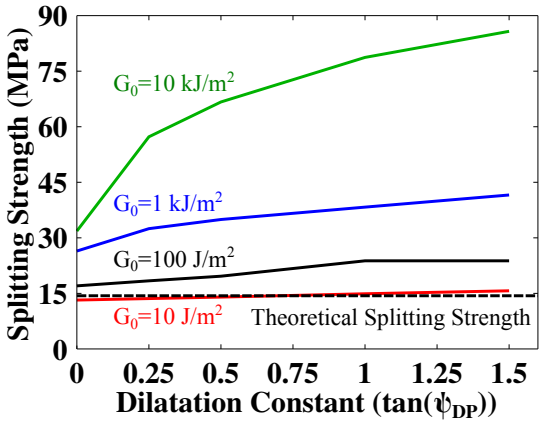

Figure 11: Splitting strength as a function of dilatation constant for cylinders with fracture energies of 10 J/m^2, 100 J/m^2, 1 kJ/m^2, and 10 kJ/m^2 plotted against the target splitting strength. Splitting strength results are found to agree with the target value for brittle and quasi-brittle fracture energies of 10 J/m^2 and 100 J/m^2. As the fracture energy is further increased, deviation from the target strength is observed.

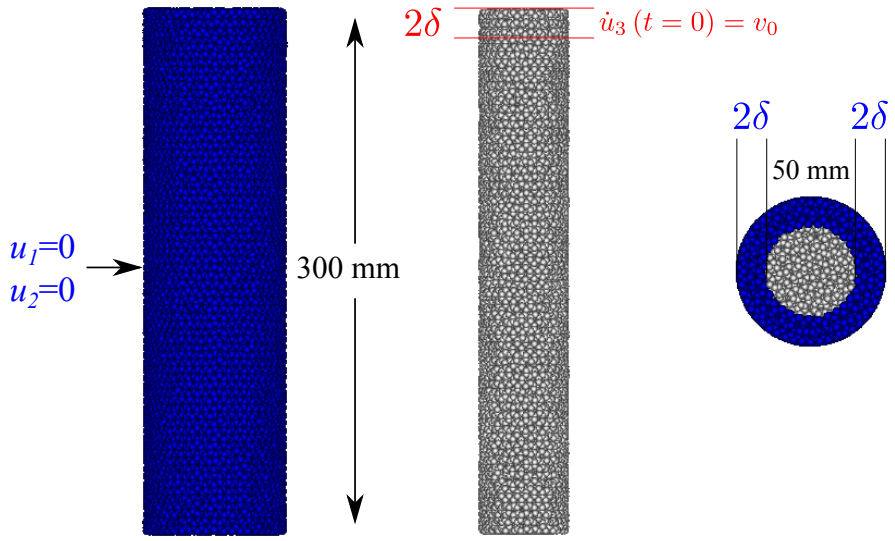

Figure 12: Model configuration for low velocity impact simulations used to calculate spall depth and strength.

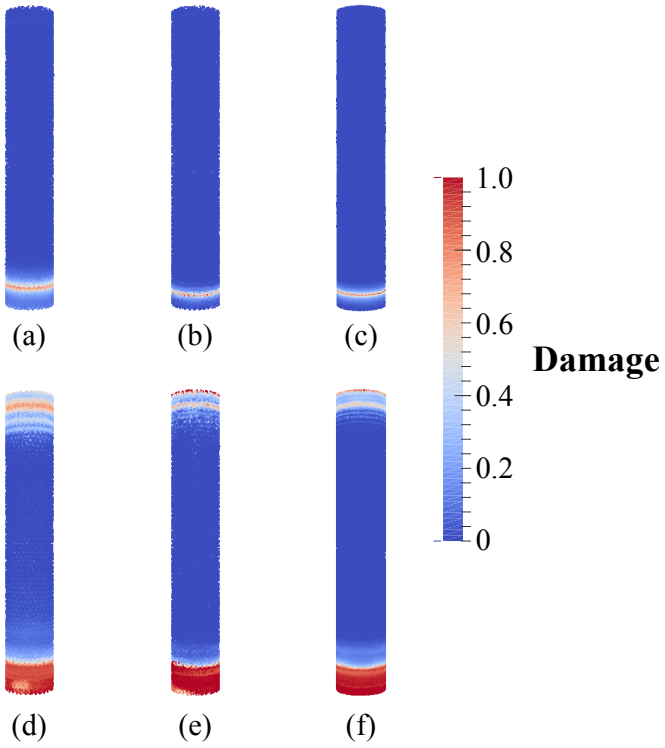

Figure 13: Visualization of the damage field after impact and spallation for, (a) δ=15 mm, dx=5 mm, v_0=10 m/s; (b) δ=7.5 mm, dx=5 mm, v_0=10 m/s; (c) δ=7.5 mm, dx=2.5 mm, v_0=10 m/s; (d) δ=15 mm, dx=5 mm, v_0=50 m/s; (e) δ=7.5 mm, dx=5 mm, v_0=50 m/s; and (f) δ=7.5 mm, dx=2.5 mm, v_0=50 m/s reveals rear-face spall and fragementation at low and high impact velocities, respectively, and front-face scabbing at high impact velocities.

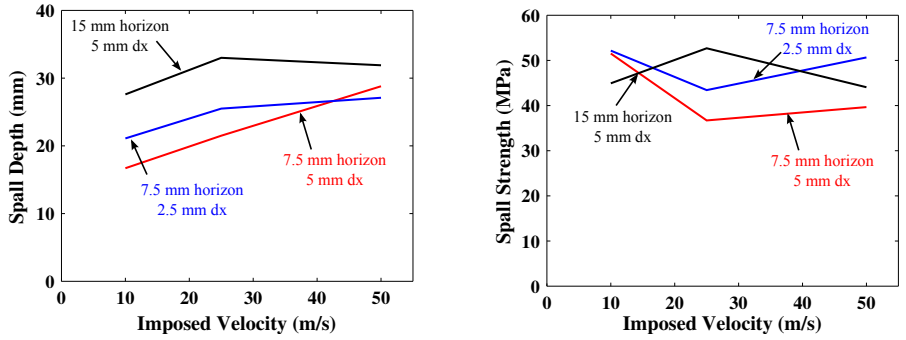

(a) (b)

Figure 14: Rear-face velocity measurements facilitate (a) Spall depth and (b) spall strength calculations for imposed velocities of 10, 25, and 50 m/s with varying horizon and grid spacing. Spall depth is found to be dependent on the peridynamic horizon, while spall strength is independent of the horizon.

5 Discussion

Free surfaces in a peridynamic simulation are subject to calculation errors since the horizon is not fully populated with material points. When the horizon is not sufficiently small in comparison to the model size, error in the effective elastic properties of the model is introduced. As the horizon is made smaller the influence of calculations performed near the surface decreases. The smallest horizon analyzed, 7.5 mm, 15% of the cylinder diameter, produced 10% in the effective elastic modulus as shown in Figure 7. Further reduction in the horizon size or increase in the cylinder diameter will result in more accurate elastic calculations. Similarly, errors will be introduced along internal voids and nascent fracture surfaces.

All horizon sizes and grid spacings produced effective compressive yield strengths within 3% of the target strength, 200 MPa. Furthermore, the friction coefficient and shear strength can be systemically varied and maintain a constant compressive strength. The scaling laws developed to relate the parameters of the peridynamic model to the classical Drucker-Prager model are shown to be correct. Poor numerical convergence is observed for high β.

The use of a dissipation-based bond failure criteria demonstrated that the effective splitting strength of the concrete cylinder was biased by the fracture energy of the material and by ψ. Simulations of cylinders with fracture energies of 10 J/m^2 and 100 J/m^2 produced splitting strengths in good agreement with the predicted strength. Fracture energies of 1 kJ/m^2 and 10 kJ/m^2 however, produced effective splitting strengths which deviated significantly from the predicted value. Increases in the dilatation constant resulted in a higher effective splitting strength. This phenomena is related to the increase in pressure due to positive plastic volumetric flow.

The modeling of impact and spall demonstrated that the spall strength is independent of the horizon size, grid spacing, and impact velocity. The spall depth is dependent on the horizon size and impact velocity, but does not exhibit dependence on the grid spacing. The implication of this result is the dependence of the spall depth on the characteristic length of the continuum, such as the size or spacing of aggregates, pores, and fibers. The peridynamic modeling is a Lagrangian formulation, i.e., the reference configuration is used to calculate the extension state at all future deformed configurations. As a result, peridynamics is not well-suited for high-velocity impacts that induce large plastic deformations and limited fracture, i.e., ballistic impact of ductile metals such as steel. It is aptly suited for low-velocity impact of brittle and quasi-britle materials such as concrete, where failure is dictated by the strength and fracture properties of the material.

Peridynamics facilitates modeling of large deformations involving fracture, inclusion of non-locality due to underlying microstructure, convergence of dissipative processes during fracture, and material heterogeneity in a single, mathematically consistent framework. Plasticity and fracture arise organically through the equations of motion of the material points. These attributes are necessary to model concrete during failure, yet are not provided by finite element methods (FEM) [Holmquist et al., 1993], cohesive FEM [Mota et al., 2003], extended

FEM [Mos and Belytschko, 2002], Eulerian formulations [Fahrenthold and Yew, 1995], or particle methods such as smoothed particle hydrodynamics [Johnson et al., 1996] or reproducing kernel particle method [Chen and Gunzburger, 2011]. Peridynamics, thus, offers distinct advantages over other techniques when modeling dynamic fracture in non-local, pressure-dependent, quasi-brittle materials such as concrete.

Peridynamics offers advantages over other theoretical frameworks and modeling methodologies, however, these advantages come with a computational cost. The computational cost of the pressure-dependent plasticity model is compared to that of the classical Drucker-Prager model using finite element method. The cylinder compression model is used with nominal node and material point spacings of 5 mm. Compression was modeled until a strain of 0.004, ensuring that the cylinder was fully plastic. The computational cost of the FEM model was 0.6 CPU-hours, while the computational cost of the peridynamic model was 24 CPU-hours, i.e., the peridynamic model has approximately 40$\times$ the computational cost of the FEM model. It is recommended that pressure-sensitive plasticity model only be used to solve engineering problems involving fracture, particularly under tensile loading conditions where classical techniques do not yield convergence of plastic strain or dissipation [Belytschko et al., 1986].

6 Anticipated Impact

The theoretical framework and modeling capability developed herein expands the number of materials that can be modeled using peridynamics to include pressure-dependent solids such as rock, concrete, ceramics, and granular materials. An intrinsic material length is incorporated in the peridynamic theory, the horizon. The horizon size is a material property dependent on the underlying structure, or heterogeneity. The size and spacing of the reinforcing phases in concrete is on the order of millimeters, thus, an intelligently chosen engineering-scale horizon will reflect the characteristic dimension of these phases.

The next step in modeling heterogeneous, pressure-dependent materials such as concrete using peridynamics is the development of a heirarchical multi-scale modeling methodology. The peridynamic horizon naturally serves as the dimension that "links" neighboring length scales. An example of two length scales linked via the horizon is shown in Figure 15. The horizon at Scale 0 corresponds to the domain size at Scale 1. In this example, at Scale 1 reinforcing phases in the form of fibers and aggregate are illustrated.

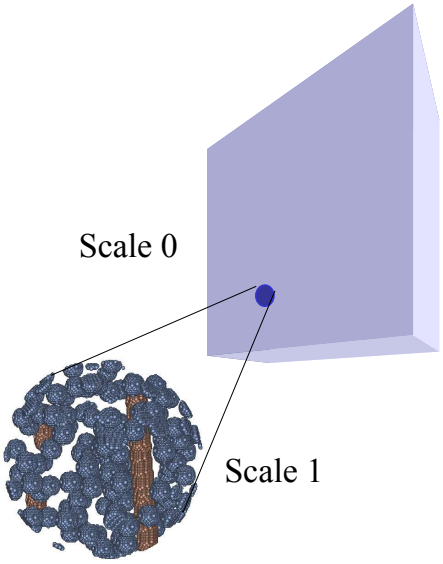

Figure 15: Multi-scale peridynamic horizon utilizing the peridynamic horizon to link the engineering scale, Scale 0, to the scale of the reinforcing phases, Scale 1.

Peridynamic modeling at Scale 1 facilitates the:

1. Calculation of $\underline{\mathbf{Y}}$ enriched with fine-scale degrees of freedom;
2. Calculation of effective elastic constants α and k;
3. Calculation of effective plasticity model parameters t_0, β, and ψ; and
4. Determination of crack nucleation and propagation characteristics as well as the deformation mechanisms leading to failure.

The internal damage within a fine scale structure consisting of 2% pores by volume 2 mm in diameter, loaded in tension and shear, is visualized in Figure 16. In tension, multiple interacting fracture process zones are observed. Under shear loading, a single critical fracture process zone is observed. For both loading conditions, initiation and propagation of the fracture process zone is observed to occur at pores and along planes intersecting pores, respectively.

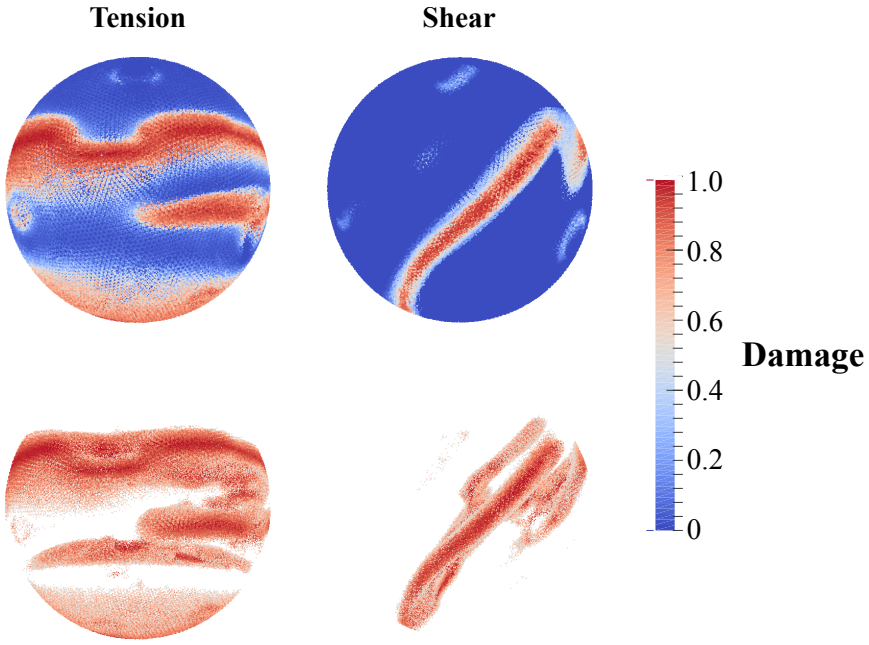

Figure 16: Peridynamic modeling at Scale 1 facilitates the determination of crack nucleation and propagation characteristics as well as the deformation mechanisms leading to failure in a concrete microstructure consisting of 2% pore by volume. The development of multiple fracture process zones is observed in tension; a single critical fracture process zone forms under shear loading.

Using the pressure-dependent peridynamic plasticity model developed herein as a starting point, it is proposed that a systematic evaluation of the model be performed to determine its accuracy for modeling impact, spall, and penetration of a variety of pressure-dependent materials. Direct comparison to existing models that accurately these phenomena should be performed. Evaluation metrics should include and not be limited to: spall strength, spall depth, fragment size distribution, residual velocity, fracture patterns, and computational cost.

After thorough evaluation of the peridynamic plasticity model against currently implemented models, a hierarchical multi-scale modeling methodology to calculate and determine the 4 points above will be formalized. Calculation of the multi-scale kinematics and effective elastic and inelastic properties will be performed on a single material system of interest. The study will include a parametric analysis of the effect of the geometry and volume of fine-scale structure on engineering-scale properties. The results will facilitate material design for tailored properties.

7 Conclusion

A pressure-dependent peridynamic plasticity model was formulated. Scaling laws were derived to directly relate the parameters of the model to the parameters of the classical Drucker-Prager plasticity model. Thermodynamic analysis of the material model shows adherence to the Dissipation Inequality for associated plastic flow. Unit tests, consisting of two material points and two peridynamic bonds, were conducted to verify the accuracy of the implicit integration algorithm used to calculate the plastic extension state and force state at every time step. A dissipation-based bond failure criteria was coupled to the constitutive model so that bond failure only occurs after yielding. The simulation of compression, splitting, and low velocity impact of concrete structures confirms the accuracy of the model for simulating pressure-dependent quasi-brittle materials, such as concrete. The peridynamic model addresses the need of pressure-dependency, non-locality due to underlying microstructure, convergence of dissipative processes during fracture, and material heterogeneity in a single, mathematically consistent framework, thus, offering advantages over other theories and modeling methodologies. The work expands the types of materials that can be modeled using peridynamics. A multi-scale methodology for simulating concrete to be used in conjunction with the plasticity model was presented.

This page intentionally left blank.

References

Agwai, Abigail, Guven, Ibrahim, Madenci, Erdogan, 2011. Predicting crack propagation with peridynamics: a comparative study. International Journal of Fracture 171, 65–78.
URL http://dx.doi.org/10.1007/s10704-011-9628-4

Askari, Abe, Nelson, Karl, Weckner, Olaf, Xu, Jifeng, Silling, Stewart, 2011. Hail impact characteristics of a hybrid material by advanced analysis techniques and testing. Journal of Aerospace Engineering 24 (2), 210–217.
URL http://link.aip.org/link/?QAS/24/210/1

ASTM, 2009. C496 standard test method for splitting tensile strength of cylindrical concrete specimens.

Bazant, Z., Jirsek, M., 2002. Nonlocal integral formulations of plasticity and damage: Survey of progress. Journal of Engineering Mechanics 128 (11), 1119–1149.
URL

Bazant, Z., Lin, F., 1988a. Nonlocal smeared cracking model for concrete fracture. Journal of Structural Engineering 114 (11), 2493–2510.
URL

Bazant, ZdenkP., Oh, B.H., 1983. Crack band theory for fracture of concrete. Matriaux et Construction 16 (3), 155–177.
URL http://dx.doi.org/10.1007/BF02486267

Bazant, Z., Pijaudier Cabot, G., 1989. Measurement of characteristic length of nonlocal continuum. Journal of Engineering Mechanics 115 (4), 755–767.
URL

Bazant, Z., Tabbara, M., Kazemi, M., PijaudierCabot, G., 1990. Random particle model for fracture of aggregate or fiber composites. Journal of Engineering Mechanics 116 (8), 1686–1705.
URL

Bazant, Z. P.ant, Zdenk. P., Lin, Feng-Bao, 1988b. Non-local yield limit degradation. International Journal for Numerical Methods in Engineering 26 (8), 1805–1823.
URL http://dx.doi.org/10.1002/nme.1620260809

Belytschko, Ted, Baant, Zdenk P., Yul-Woong, Hyun, Ta-Peng, Chang, 1986. Strain-softening materials and finite-element solutions. Computers & Structures 23 (2), 163 – 180.
URL http://www.sciencedirect.com/science/article/pii/0045794986902105

Chen, X., Gunzburger, Max, 2011. Continuous and discontinuous finite element methods for a peridynamics model of mechanics. Computer Methods in Applied Mechanics and Engineering 200 (9-12), 1237 – 1250.
URL http://www.sciencedirect.com/science/article/pii/S0045782510002926

di Prisco, M., Mazars, J., 1996. Crush-crack': a non-local damage model for concrete. Mechanics of Cohesive-frictional Materials 1 (4), 321–347.
URL http://dx.doi.org/10.1002/(SICI)1099-1484(199610)1:4<321::AID-CFM17>3.0.CO;2-2

Eringen, A.Cemal, 1981. On nonlocal plasticity. International Journal of Engineering Science 19 (12), 1461 – 1474.
URL http://www.sciencedirect.com/science/article/pii/0020722581900720

Fahrenthold, E.P., Yew, C.H., 1995. Hydrocode simulation of hypervelocity impact fragmentation. International Journal of Impact Engineering 17 (13), 303 – 310.
URL http://www.sciencedirect.com/science/article/pii/0734743X9599856M

Ferrara, L., Prisco, M., 2001. Mode i fracture behavior in concrete: Nonlocal damage modeling. Journal of Engineering Mechanics 127 (7), 678–692.
URL

Foster, John, Silling, Stewart A., Chen, Weinong, 2011. An energy based failure criterion for use with peridynamic states. International Journal for Multiscale Computational Engineering 9 (6), 675–688.

Gerstle, W., Sau, N., Silling, S., 2007. Peridynamic modeling of concrete structures. Nuclear Engineering and Design 237 (1213), 1250 – 1258.

Grassl, Peter, Jirsek, Milan, 2006. Plastic model with non-local damage applied to concrete. International Journal for Numerical and Analytical Methods in Geomechanics 30 (1), 71–90.
URL http://dx.doi.org/10.1002/nag.479

Ha, Youn, Bobaru, Florin, 2010. Studies of dynamic crack propagation and crack branching with peridynamics. International Journal of Fracture 162, 229–244.
URL http://dx.doi.org/10.1007/s10704-010-9442-4

Ha, Youn Doh, Bobaru, Florin, 2011. Characteristics of dynamic brittle fracture captured with peridynamics. Engineering Fracture Mechanics 78 (6), 1156 – 1168.
URL http://www.sciencedirect.com/science/article/pii/S0013794410004959

Hillerborg, A., Moder, M., Petersson, P.-E., 1976. Analysis of crack formation and crack growth in concrete by means of fracture mechanics and finite elements. Cement and Concrete Research 6 (6), 773 – 781.
URL http://www.sciencedirect.com/science/article/pii/0008884676900077

Holmquist, T.J., Johnson, G.R., Cook, W.H., 1993. A computational constitutive model for concrete subjected to large strains, high strain rates, and high pressures. In: Murphy, M.J., Backofen, J.E. (Eds.), Proceedings of the 14th international symposium on ballistics, American Defense Preparedness Association (ADPA). p. 591600.

Hu, Wenke, Wang, Yenan, Yu, Jian, Yen, Chian-Fong, Bobaru, Florin, 2013. Impact damage on a thin glass plate with a thin polycarbonate backing. International Journal of Impact

Engineering 62 (0), 152 – 165.
URL http://www.sciencedirect.com/science/article/pii/S0734743X13001395

Huang, Dan, Zhang, Qing, Qiao, PiZhong, 2011. Damage and progressive failure of concrete structures using non-local peridynamic modeling. SCIENCE CHINA Technological Sciences 54, 591–596.
URL http://dx.doi.org/10.1007/s11431-011-4306-3

Johnson, Gordon R., Stryk, Robert A., Beissel, Stephen R., 1996. Sph for high velocity impact computations. Computer Methods in Applied Mechanics and Engineering 139 (14), 347 – 373.
URL http://www.sciencedirect.com/science/article/pii/S0045782596010894

Macek, Richard W., Silling, Stewart A., 2007. Peridynamics via finite element analysis. Finite Elements in Analysis and Design 43 (15), 1169 – 1178.
URL http://www.sciencedirect.com/science/article/pii/S0168874X07001035

Millon, O., Riedel, W., Thoma, K., Fehling, E., Noldgen, M., 2009. Fiber-reinforced ultra-high performance concrete under tensile loads. In: DYMAT 2009. pp. 671–677.

Mitchell, John A., May 2011. A nonlocal, ordinary, state-based plasticity model for peridynamics. Sandia National Laboratories, Albuquerque, NM, Sandia Report SAND2011-3166.

Mota, A., Klug, W. S., Ortiz, M., Pandolfi, A., 2003. Finite-element simulation of firearm injury to the human cranium. Computational Mechanics 31 (1-2), 115–121.
URL http://dx.doi.org/10.1007/s00466-002-0398-8

Mos, Nicolas, Belytschko, Ted, 2002. Extended finite element method for cohesive crack growth. Engineering Fracture Mechanics 69 (7), 813 – 833.
URL http://www.sciencedirect.com/science/article/pii/S001379440100128X

Needleman, A., 1988. Material rate dependence and mesh sensitivity in localization problems. Computer Methods in Applied Mechanics and Engineering 67 (1), 69 – 85.
URL http://www.sciencedirect.com/science/article/pii/0045782588900692

Oterkus, E., Barut, A., Madenci, E., 2012. Peridynamics based on principle of virtual work. Cited By (since 1996)1.
URL http://www.scopus.com/inward/record.url?eid=2-s2.0-84881382062partnerID=40md5=b9f0

Parks, M.L., Littlewood, D.J., Mitchell, J.A., Silling, S.A., 2012. Peridigm users guide. Sandia National Laboratories, Report.

Planas, J., Guinea, G.V., Elices, M., 1996. Basic issues on nonlocal models: Uniaxial modeling. Departamento de Ciencia de Materiales, ETS de Ingenieros de Caminos, Univ. Polite cnica de Madrid, Ciudad Univ. sn., 28040 Madrid, Spain., Report 96-jp03.

Silling, S., 2000. Reformulation of elasticity theory for discontinuities and long-range forces. Journal of the Mechanics and Physics of Solids 48 (1), 175 – 209.

Silling, S., 2010. Linearized theory of peridynamic states. Journal of Elasticity 99, 85–111.
URL http://dx.doi.org/10.1007/s10659-009-9234-0

Silling, S.A., Askari, E., 2005. A meshfree method based on the peridynamic model of solid mechanics. Computers & Structures 83 (17-18), 1526 – 1535.

Silling, S., Epton, M., Weckner, O., Xu, J., Askari, E., 2007. Peridynamic states and constitutive modeling. Journal of Elasticity 88, 151–184.

Silling, S.A., Lehoucq, R.B., 2010. Peridynamic theory of solid mechanics. In: Aref, Hassan, van der Giessen, Erik (Eds.), Advances in Applied Mechanics. Vol. 44 of Advances in Applied Mechanics. Elsevier, pp. 73 – 168.
URL http://www.sciencedirect.com/science/article/pii/S0065215610440028

Sorelli, Luca, Constantinides, Georgios, Ulm, Franz-Josef, Toutlemonde, Franois, 2008. The nano-mechanical signature of ultra high performance concrete by statistical nanoindentation techniques. Cement and Concrete Research 38 (12), 1447 – 1456.
URL http://www.sciencedirect.com/science/article/pii/S0008884608001567

Strmberg, Lena, Ristinmaa, Matti, 1996. Fe-formulation of a nonlocal plasticity theory. Computer Methods in Applied Mechanics and Engineering 136 (12), 127 – 144.
URL http://www.sciencedirect.com/science/article/pii/0045782596009978

Xu, Jifeng, Askari, Abe, Weckner, Olaf, Silling, Stewart, 2008. Peridynamic analysis of impact damage in composite laminates. Journal of Aerospace Engineering 21 (3), 187–194.
URL http://link.aip.org/link/?QAS/21/187/1

DISTRIBUTION:

1 M. Zhou
George W. Woodruff School of Mechanical Engineering
Georgia Institute of Technology
801 Ferst Dr. NW
Atlanta, GA 30332

1 J. Foster
Petroleum and Geosystems Engineering
University of Texas - Austin
200 E. Dean Keeton St., Stop C0300
Austin, TX 78712-1585

1 MS 1322 S. Silling, 1444
1 MS 1320 M. Parks, 1442
1 MS 1320 R. Lehoucq, 1442
1 MS 0840 H. E. Fang, 1554
1 MS 1322 D. Littlewood, 1444
1 MS 1322 J. Mitchell, 1444
1 MS 9042 J. Ostien, 8256
1 MS 9042 T. Vogler, 8256
1 MS 0899 Technical Library, 9536 (electronic copy)

Sandia National Laboratories